







Spiral band structure hidden in the bulk chiral crystal NbSi₂

Cheng Zhang ¹, Tatsuya Shishidou ², Ryoga Amano,³ Koji Miyamoto,⁴ Taisei Sayo,³ Chiho Shimada,³ Yusuke Kousaka ³, Michael Weinert ², Yoshihiko Togawa ^{3,5} and Taichi Okuda ^{4,*}

¹Graduate School of Advanced Science and Engineering, Hiroshima University, 131 Kagamiyama, Higashi-Hiroshima 739-8526, Japan

²Department of Physics, University of Wisconsin-Milwaukee, Milwaukee, Wisconsin 53201, USA

³Department of Physics and Electronics, Osaka Metropolitan University, Osaka 599-8531, Japan

⁴Hiroshima Synchrotron Radiation Center (HiSOR), Hiroshima University, 2-313 Kagamiyama, Higashi-Hiroshima 739-0046, Japan

⁵Quantum Research Center for Chirality, Institute for Molecular Science, Okazaki 444-8585, Japan



(Received 30 July 2023; accepted 20 November 2023; published 21 December 2023)

The electronic structure of chiral crystal NbSi₂ is investigated using angle-resolved photoelectron spectroscopy and density-functional theory calculations. In addition to the observation of clear band dispersions over a wide energy range, unexpected spiral-shaped constant energy contours (CECs) are found at specific binding energies. The rotation direction of this spiral signal is reversed in crystals having opposite chirality, indicating that the observed CECs originate from the structural chirality. Our theoretical analysis suggests that a combination of the bulk chiral atomic arrangement and surface states that penetrate sufficiently deep into the bulk is the key to understanding the emergence of spiral CECs.

DOI: [10.1103/PhysRevB.108.235164](https://doi.org/10.1103/PhysRevB.108.235164)

I. INTRODUCTION

Chirality, the mirror asymmetry of an object [1], is widespread in nature and plays an important role in many phenomena in physics, chemistry, and biology [2,3], including different pharmacological activities of enantiomers of some chiral drugs (such as *R*- and *S*-thalidomide) [4,5], and the homochirality of biomolecules (L-amino acids and D-sugars) [6–8]. In condensed matter physics, chiral materials have also been intensively studied since chirality leads to interesting physical phenomena, e.g., the peculiar hedgehoglike radial spin texture in Te crystals [9,10], and the anomalous magnetic breakdown effect of TaSi₂ crystal [11,12].

Recently, the so-called chirality-induced spin selectivity (CISS) effect, in which a spin-polarized current is generated when a current is passed through a material with a chiral structure, has been observed in some chiral molecules [13,14], and is attracting attention because of its potential in spintronics applications [15]. The first indication of the CISS was obtained from low-energy photoemission of L- or D-stearyl lysine thin films deposited on the surface of a polycrystalline gold substrate [16,17] by the Langmuir-Blodgett method [18–20]. Similar measurements have also been done with double stranded DNA where CISS was directly observed using a Mott polarimeter [21]. Later, the CISS was also verified in various transport experiments [22–26].

The relation between the electronic state and the appearance of CISS has not yet been well understood; the microscopic mechanism of the production of spin-polarized electrons is still controversial, although various models and possible origins have been proposed, such as the spin-orbit coupling (SOC) of substrates [27], spin asymmetric multiple

scattering [28], topological orbital texture [29], and various theoretical analyses based on the tight-binding model [30–34].

Besides the organic molecules mentioned above, the CISS effect has been observed in transport measurements (utilizing the inverse spin Hall effect) in the bulk inorganic materials NbSi₂ and TaSi₂ [35,36]. A recent theoretical paper [37] suggested that the CISS signal of these materials can be attributed to the spin accumulation generated by the collinear Rashba-Edelstein effect (REE). In addition, it is predicted that the NbSi₂ and TaSi₂ possess Kramers-Weyl fermions in which the Weyl SOC term may also contribute to the robustness of the spin-polarized current in these materials [37]. However, no experimental verification has been done to support that scenario yet.

The robust and stable bulk single crystals of NbSi₂ or TaSi₂ provide the opportunity to experimentally examine the mechanism of the CISS—and the effects of chirality—from the electronic structure point of view, thereby complementing the transport and structural studies of these classes of materials. However, since the crystal has no cleavage planes in these materials, it is difficult to get an atomically flat surface as required for the angle-resolved photoelectron spectroscopy (ARPES) measurements, and only the bulk Fermi surfaces deduced by the de Haas-van Alphen effect [38] and limited photoemission results [39] have been reported so far.

In this paper, we report our observation of the electronic structure of NbSi₂ by ARPES, which is in reasonably good agreement with the previously reported density-functional theory (DFT) calculation [40]. Interestingly, however, we also find unexpected spiral photoelectron distribution patterns whose rotation direction depends on the structural chirality. By means of DFT calculations and symmetry considerations, we demonstrate that the spiral pattern can emerge from the intrinsic band structure, without invoking final state effects in the photoemission process; in particular, we demonstrate

*Corresponding author: okudat@hiroshima-u.ac.jp

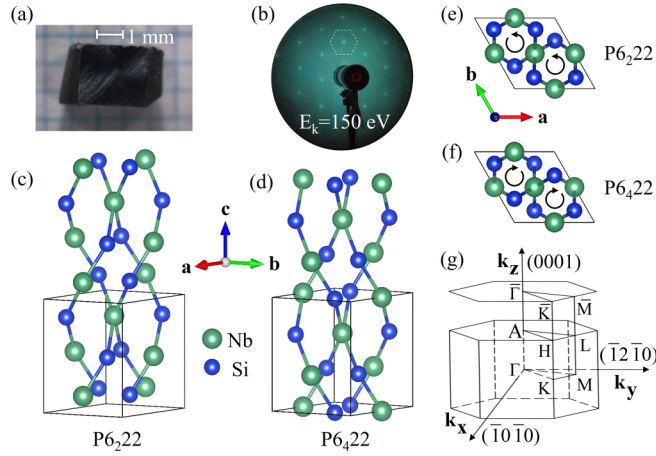


FIG. 1. (a) Right-handed NbSi_2 crystal surface after mechanical polishing. (b) LEED pattern of the polished surface (a) after annealing ($\sim 1000^\circ\text{C}$) and Ar ion sputtering ($\sim 150\text{ V}$). (c)–(f) Top and side views of the structures of two chiral crystals; the primitive cells are marked in black lines and the black arrows indicate the direction of the chiral atomic arrangement along the c axis. (g) The 3D BZ of NbSi_2 and its projection onto the (0001) surface.

that the inherent bulk chirality and surface states that extend several layers into the bulk are essential ingredients that lead to the profound spiral pattern.

II. METHODS

The chiral transition-metal disilicide NbSi_2 single crystal was grown using a laser diode heated floating zone (LDFZ) method [41]. Figures 1(c)–1(f) show the crystal structures of right- ($P6_22$) and left-handed ($P6_422$) NbSi_2 that have opposite chirality along the c axis. The clean and atomically flat (0001) surfaces were obtained by cycles of Ar ion sputtering and annealing after mechanical polishing of the sample [Fig. 1(a)], after which a sharp low-energy electron diffraction (LEED) pattern was successfully observed [Fig. 1(b)].

ARPES measurements were performed at beamline BL-9B of HiSOR. The base pressure of the analysis chamber where the cryogenic six-axis goniometer is installed was kept $\sim 10^{-9}$ Pa, and the sample temperature was set to around 35 K. The horizontally polarized light from an APPLE-II type variable polarization undulator impinges the sample at 50° from the surface normal. The photon energy was set as 50 eV. The ARPES data were taken with a Scienta Omicron R4000 analyzer, with energy (angular) resolution of about 40 meV (0.2°).

The DFT calculations for the bulk and (0001) surface of NbSi_2 were performed using the Vienna *Ab initio* Simulation Package [42] with pseudopotentials from the projector augmented wave method [43,44], Perdew-Burke-Ernzerhof [45] exchange correlation, and with SOC included. The (0001) surface was modeled by a repeated slab of 23 NbSi_2 atomic layers with 24 Å vacuum. The experimental structural parameters [46] were adopted. A $20 \times 20 \times 20$ ($\times 1$) Γ -centered k -point mesh was used during the self-consistent field cycle to sample the bulk three-dimensional (3D) [slab two-dimensional (2D)] Brillouin zone (BZ). In calculating

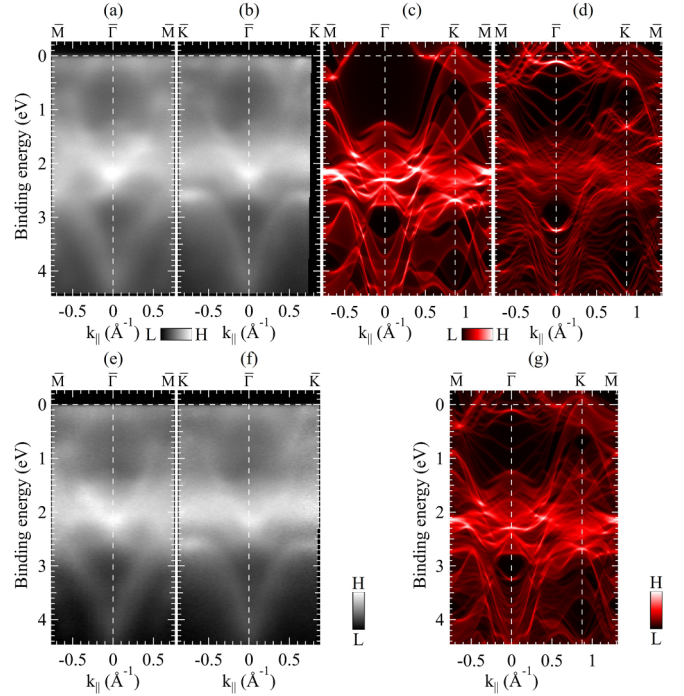


FIG. 2. (a), (b) ARPES band structures of right-handed NbSi_2 crystal along the $\bar{M} - \bar{\Gamma} - \bar{M}$ and $\bar{K} - \bar{\Gamma} - \bar{K}$ directions. (c), (d) Bulk and slab band structure calculated along the high-symmetry lines $\bar{M} - \bar{\Gamma} - \bar{K} - \bar{M}$. For the bulk, the k_z dependence is projected onto the 2D BZ by plotting the bands on 50 evenly spaced planes along k_z . For the slab, the top two layers' contribution is shown. (e), (f) ARPES bands for left-handed crystal along the $\bar{M} - \bar{\Gamma} - \bar{M}$ and $\bar{K} - \bar{\Gamma} - \bar{K}$ directions. (g) Mixture of bulk (60%) and slab (40%) calculated band structures of right-handed NbSi_2 crystal along high-symmetry lines.

the 2D CECs, a denser in-plane k -point mesh of 100×100 was used to generate Kohn-Sham orbitals, and a plane wave energy cutoff of 400 eV was used. The layer-projection technique [47] was used in considering the finite mean free path (MFP) of photoelectrons. Note there are three (0001) surface terminations (Fig. 1), related to each other by threefold screw rotation. To have a better comparison with the experiments, we averaged the results of the three terminations in the slab band dispersion and slab CEC plots, which results in a sixfold symmetry of the surface signals in the 2D BZ. This suggests that there likely exist three domains (three different terminations) in the samples as prepared, and that the domain size of each is large enough to lead to clear energy band dispersions.

III. RESULTS AND DISCUSSION

Figures 2(a) and 2(b) show the energy band structure of the right-handed NbSi_2 crystal experimentally observed by ARPES along the high-symmetry lines $\bar{M} - \bar{\Gamma} - \bar{M}$ and $\bar{K} - \bar{\Gamma} - \bar{K}$ at $h\nu = 50\text{ eV}$. Many bands are clearly observed, indicating the high quality of the sample surface. The dispersions along different directions ($\bar{M} - \bar{\Gamma} - \bar{M}$, $\bar{K} - \bar{\Gamma} - \bar{K}$) have similar outlines to each other. For example, an upward parabolic band is observed with minimum binding energy (E_B) of $\sim 4.4\text{ eV}$ at the $\bar{\Gamma}$ point, becoming relatively flat around $E_B = 2.6\text{ eV}$. At around $E_B = 2.0\text{ eV}$ at the $\bar{\Gamma}$ point

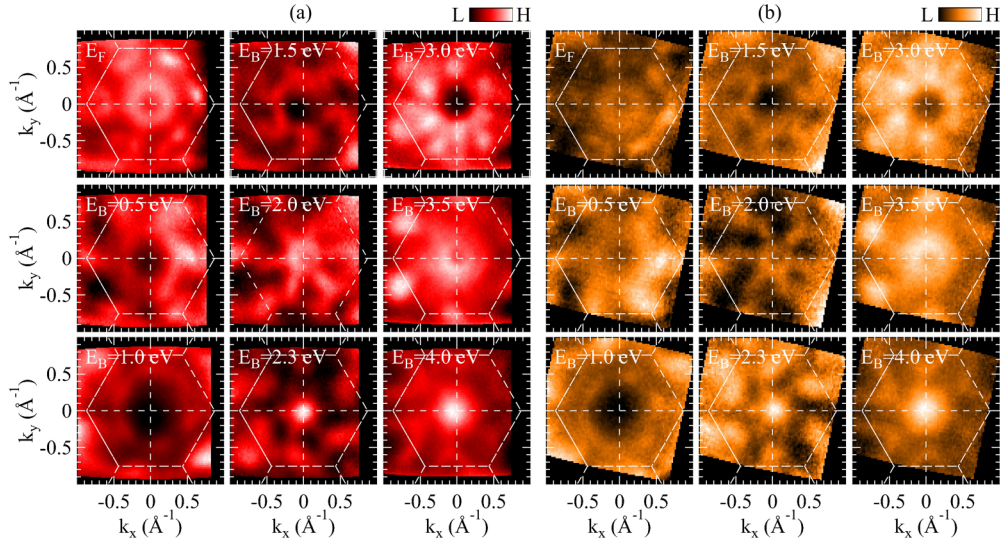


FIG. 3. ARPES CECs for the (a) right- and (b) left-handed NbSi₂, at different E_B through an $E(k_x, k_y)$ data set obtained at $h\nu = 50$ eV.

some strong intensities with relatively flat dispersion are also observed. In addition, some metallic bands which clearly cut the Fermi level near $\bar{\Gamma}$ are also observed along both the $\bar{\Gamma} - \bar{M}$ and $\bar{\Gamma} - \bar{K}$ lines, consistent with the metallic character of the NbSi₂. On closer inspection, however, the above-mentioned parabolic band is slightly steeper along the $\bar{K} - \bar{\Gamma} - \bar{K}$ line, which extends to a relatively flat band in the range of smaller wave vectors; i.e., the band has a small anisotropy.

The bulk DFT calculation along $\bar{M} - \bar{\Gamma} - \bar{K} - \bar{M}$ is shown in Fig. 2(c), where the SOC is taken into account and the k_z dependence is projected onto the 2D BZ. The calculation basically reproduces the profiles and trends of the experimental bands: the upward parabolic band starting at about $E_B = 4.0$ eV, the relatively flat band at around $E_B = 2.0$ eV, and the metallic bands in the vicinity of the \bar{K} and \bar{M} points (the calculated Fermi energy is shifted down by 0.18 eV to better correspond to the experimental result.). Furthermore, the large theoretical spectral weights near the high-symmetry points, e.g., at $E_B = 2.15$ eV at \bar{M} , $E_B = 2.2$ eV at $\bar{\Gamma}$, and $E_B = 2.65$ eV at \bar{K} , in the calculation are also observed experimentally. However, the strong metallic bands near $\bar{\Gamma}$ along both the $\bar{\Gamma} - \bar{K}$ and $\bar{\Gamma} - \bar{M}$ lines in the experiment are not reproduced.

This discrepancy is explained by the (0001) surface slab calculation, Fig. 2(d), where the contributions from the top two surface layers are shown. The slab calculation fairly reproduces the experimentally observed metallic bands near $\bar{\Gamma}$, as well as halfway along $\bar{\Gamma} - \bar{M}$ and $\bar{\Gamma} - \bar{K}$. Therefore, these metallic bands are likely due to the surface states. On the other hand, the other surface states at $E_B = 3.2$ eV at the $\bar{\Gamma}$ point in the slab calculation are not observed in our experiment, which might be due to the matrix element effect of the photoemission process.

In order to see the electronic structure in more detail, we measured constant energy contours (CECs) over the 2D BZ at different binding energies. Figure 3(a) shows the result for the right-handed NbSi₂. These CECs all roughly have a six-fold geometry, consistent with the hexagonal LEED pattern, Fig. 1(b).

However, unexpectedly, we found that some CECs show a spiral structure. The most prominent one can be seen at $E_B = 1.5$ eV; a spiral with six wings is turning counterclockwise. The clarity of the spiral structures, Fig. 3(a), depends on E_B ; for example, the clear spiral pattern at $E_B = 1.5$ eV, the relatively clear spiral pattern at $E_B = 0.5$ eV (or 2.0, 2.3, and 3.0 eV), the faint spiral pattern at E_F (or $E_B = 1.0$, and 3.5 eV), and the almost negligible spiral pattern at $E_B = 4.0$ eV (see also the Supplemental Material [48]).

The fact that NbSi₂ is a chiral crystal raises the question of whether the spiral structures observed in the CECs could be attributed to its chirality. To examine this hypothesis, a left-handed NbSi₂ crystal was also measured by ARPES. In the measurement, Figs. 2(e) and 2(f), clear band dispersions are also obtained and typical CECs are shown in Fig. 3(b). Obviously, these CECs also have a spiral structure with E_B dependence similar to those of right-handed crystals, but their rotation direction is opposite. Therefore, we can conclude that the spiral CECs originate from the crystal chirality.

To investigate the origin of the spiral CECs, we calculated the constant energy cuts of the bulk band structure, Fig. 4(a), of right-handed NbSi₂. These calculated bulk CECs, however, do not show any spiral structure. The ideal bulk crystal ($P6_222$ or $P6_422$), has, in addition to the sixfold axis, the twofold rotation axes as well. Combined with time-reversal symmetry T , each of the twofold symmetries acts as a mirror symmetry in reciprocal space. For instance, it is easy to show for the twofold rotation about the x axis,

$$TC_{2x} \begin{bmatrix} k_x \\ k_y \\ k_z \end{bmatrix} = T \begin{bmatrix} k_x \\ -k_y \\ -k_z \end{bmatrix} = \begin{bmatrix} -k_x \\ k_y \\ k_z \end{bmatrix},$$

so that the combined TC_{2x} acts as a mirror reflection M_x . The effective mirror symmetry in k space leaves no room for spiral structures to emerge. To account for the spiral CECs, we need to break the in-plane twofold symmetry. This is naturally realized at the material's (0001) surface, and thus the spiral CECs might be built up by surface states and surface resonance states.

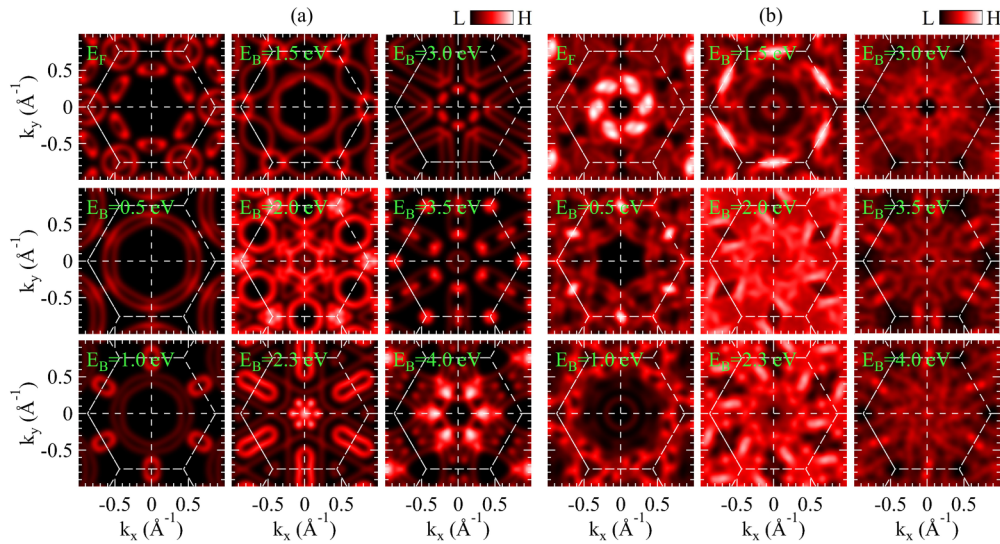


FIG. 4. Calculated (a) bulk CECs ($k_z = 0.1 \times 2\pi/c$) and (b) slab CECs of the (0001) surface of right-handed NbSi₂. The white dotted hexagons are the projection of the BZ onto the (0001) plane; cf. Fig. 1(g).

In order to verify this hypothesis, we compute CECs from the slab calculation. The slab CECs of right-handed NbSi₂, where all k_z of bulk states are projected onto the 2D BZ, are shown in Fig. 4(b); since the photoemission measurement is surface sensitive, we summed up each layer's contribution with the weight of $\exp(-z/d)$, where z and d represent the depth of each layer and the MFP of electrons, respectively. The parameter d is set as 5 Å from the so-called universal curve of MFP considering the photon energy of 50 eV in our experiment.

Some of the calculated CECs show clear spiral structures. For example, the pattern at $E_B = 1.5$ eV reproduces almost perfectly the experimental result. In addition, relatively clear spiral shapes are also obtained at some other E_B (at E_F , 0.5, 2.0, 2.3, and 4.0 eV) but almost no spiral shape is obtained at other energies. This E_B dependence of the clarity of the spiral shape is also in fairly good agreement with the experiment, suggesting that the spiral pattern is due to the surface layer contribution. Note that the rotation direction of the spiral pattern becomes opposite for the calculations for the left-handed crystal (not shown). It is worth emphasizing that other than the surface sensitivity we do not include any final state effects such as light polarization-dependent matrix elements and atomic phase interference and that our CEC calculation demonstrates the intrinsic (ground state) electronic structure.

Figure 5 shows a representative surface-state wave function (squared) that participates in the most prominent spiral pattern for $E_B = 1.5$ eV. Nb $4d$ and Si $3p$ orbitals form a hybrid state that spreads mainly over the first three atomic layers from the surface. Having a sufficient depth profile, this wave function can detect how atoms are stacked along the c axis and show an energy dispersion that depends on the crystalline chirality.

It is worth mentioning that similar spiral (windmill)-shaped CECs have been observed very recently in an achiral layered material, 1T-TaS₂, in its charge density wave phase [49]. The origin of the windmill CECs was attributed to the Star of David cluster formation in the surface region,

which induces the in-plane structural chirality. This mechanism is apparently different from the spiral CECs of NbSi₂ where the chirality inherent in the bulk (characterized by a sixfold screw axis) is necessary to generate such patterns in the electronic structure.

However, when detailed comparisons are made across all E_B , the agreement between theory and experiment is not always satisfactory. As mentioned already, since our calculation of CECs does not take into account the photoemission process, some of the discrepancies might come from the final state effect. In addition, as this material is predicted to be a Weyl semimetal [50], possible topological Fermi arcs might contribute to the observed spiral CECs. Further experimental

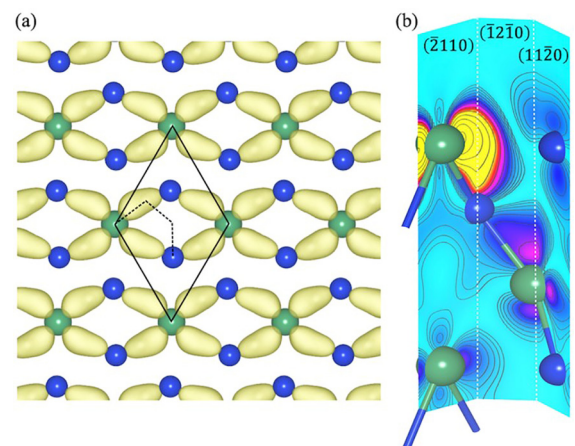


FIG. 5. A representative surface-state wave function (squared) for a k point along the $\bar{M} - \bar{\Gamma}$ line of the $E_B = 1.5$ eV spiral pattern signal. (a) Top view of surface atoms and wave function lobes (yellow). A primitive cell is indicated by the solid line. (b) Depth profile of the surface state in the perpendicular planes indicated by dotted lines in (a), i.e., $(\bar{2}110)$, $(\bar{1}\bar{2}10)$, and $(1\bar{1}\bar{2}0)$, where a chiral motif of the Nb (green)-Si (blue)-Nb bond (yellow), indicates low (moderate, high) density.

and theoretical studies in the near future are expected to address these issues.

In addition, the relation between the observed spiral CEC pattern and the CISS effect is not obvious at present. In the transport CISS effect, however, the voltage applied across the c axis may play a role analogous to the role of the surface in our spiral CECs in terms of symmetry reduction. Spin-resolved ARPES measurement will experimentally reveal the spin texture and may help to understand the relation between the CISS effect and the spin-electronic structure.

IV. CONCLUSION

We have succeeded in directly observing the chiral nature of the electronic structure of NbSi₂ by ARPES measurements. In addition to the clear energy band dispersions mostly consistent with the bulk DFT calculation, we found unexpected profound spiral-shaped photoelectron distribution patterns. Our comparative experiments on left- and right-handed single crystals, DFT calculations, and symmetry arguments reveal

that the spiral CEC patterns can be caused by the intrinsic crystal structure, i.e., the combination of the bulk chirality and surface states that can sensitively detect it, without considering the photoemission final state effects. Further studies such as spin-resolved ARPES are awaited to understand the relationship between the present findings and the origin of the CISS effect.

ACKNOWLEDGMENTS

The experiments were performed with the approval of the Proposal Assessing Committee of the Hiroshima Synchrotron Radiation Center (Proposals No. 21AU013, No. 21BG003, and No. 22AG017). This work was partly supported by KAKENHI, the Grant-in-Aid for Scientific Research (Grants No. 16H02114, No. 20H00347, No. 23H01870, and No. 23H00091) of the Japan Society for the Promotion of Science (JSPS), and by JST, the establishment of university fellowships toward the creation of science technology innovation (Grant No. JPMJFS2129). Work at UWM was supported by the National Science Foundation (EFMA-1741673).

-
- [1] W. Thomson, *Baltimore Lectures on Molecular Dynamics and the Wave Theory of Light* (Cambridge University Press, Cambridge, 2010).
- [2] M. Gardner, *The Ambidextrous Universe: Mirror Asymmetry and Time-Reversed Worlds* (Charles Scribner's Sons, New York, 1979).
- [3] L. D. Barron, Symmetry and chirality: Where physics shakes hands with chemistry and biology, *Isr. J. Chem.* **61**, 517 (2021).
- [4] S. W. Smith, Chiral toxicology: It's the same thing ... only different, *Toxicol. Sci.* **110**, 4 (2009).
- [5] Z. Y. Dong and Y. H. Ma, Atomic-level handedness determination of chiral crystals using aberration-corrected scanning transmission electron microscopy, *Nat. Commun.* **11**, 1588 (2020).
- [6] L. D. Barron, Chirality, magnetism and light, *Nature (London)* **405**, 895 (2000).
- [7] J. S. Siegel, Single-handed cooperation, *Nature (London)* **409**, 777 (2001).
- [8] E. Gibney, Force of nature gave life its asymmetry, *Nature (London)* **25**, 13 (2014).
- [9] M. Sakano, M. Hirayama, T. Takahashi, S. Akebi, M. Nakayama, K. Kuroda, K. Taguchi, T. Yoshikawa, K. Miyamoto, T. Okuda *et al.*, Radial spin texture in elemental tellurium with chiral crystal structure, *Phys. Rev. Lett.* **124**, 136404 (2020).
- [10] G. Gatti, D. Gosálbez-Martínez, S. S. Tsirkin, M. Fanciulli, M. Puppini, S. Polishchuk, S. Moser, L. Testa, E. Martino, S. Roth *et al.*, Radial spin texture of the Weyl fermions in chiral Tellurium, *Phys. Rev. Lett.* **125**, 216402 (2020).
- [11] A. Nakamura, H. Harima, M. Hedo, T. Nakama, and Y. Ōnuki, Chiral crystal structure and split Fermi surface properties in TaSi₂, *J. Phys. Soc. Jpn.* **82**, 113705 (2013).
- [12] H. Harima, T. Goho, and T. Tomit, The spin directions of the parity violated spin-splitting states in non-centrosymmetric compounds, *J. Phys.: Conf. Ser.* **592**, 012040 (2015).
- [13] R. Naaman and D. H. Waldeck, Chiral-induced spin selectivity effect, *J. Phys. Chem. Lett.* **3**, 2178 (2012).
- [14] R. Naaman and D. H. Waldeck, Spintronics and chirality: Spin selectivity in electron transport through chiral molecules, *Annu. Rev. Phys. Chem.* **66**, 263 (2015).
- [15] K. Michaeli, V. Varade, R. Naaman, and D. H. Waldeck, A new approach towards spintronics—spintronics with no magnets, *J. Phys.: Condens. Matter* **29**, 103002 (2017).
- [16] K. Ray, S. P. Ananthavel, D. H. Waldeck, and R. Naaman, Asymmetric scattering of polarized electrons by organized organic films of chiral molecules, *Science* **283**, 814 (1999).
- [17] R. Naaman and L. Sanche, Low-energy electron transmission through thin-film molecular and biomolecular solids, *Chem. Rev.* **107**, 1553 (2007).
- [18] A. Kadyshevitch and R. Naaman, Photoelectron transmission through organized organic thin films, *Phys. Rev. Lett.* **74**, 3443 (1995).
- [19] K. B. Blodgett, Films built by depositing successive monomolecular layers on a solid surface, *J. Am. Chem. Soc.* **57**, 1007 (1935).
- [20] K. B. Blodgett and I. Langmuir, Built-up films of barium stearate and their optical properties, *Phys. Rev.* **51**, 964 (1937).
- [21] B. Göhler, V. Hamelbeck, T. Markus, M. Kettner, G. Hanne, Z. Vager, R. Naaman, and H. Zacharias, Spin selectivity in electron transmission through self-assembled monolayers of double-stranded DNA, *Science* **331**, 894 (2011).
- [22] Z. T. Xie, T. Z. Markus, S. R. Cohen, Z. Vager, R. Gutierrez, and R. Naaman, Spin specific electron conduction through DNA oligomers, *Nano Lett.* **11**, 4652 (2011).
- [23] D. Mishra, T. Z. Markus, R. Naaman, M. Kettner, B. Göhler, H. Zacharias, N. Friedman, M. Sheves, and C. Fontanesi, Spin-dependent electron transmission through bacteriorhodopsin embedded in purple membrane, *Proc. Natl. Acad. Sci. USA* **110**, 14872 (2013).

- [24] O. Ben Dor, N. Morali, S. Yochelis, L. T. Baczewski, and Y. Paltiel, Local light-induced magnetization using nanodots and chiral molecules, *Nano Lett.* **14**, 6042 (2014).
- [25] H. P. Lu, J. Y. Wang, C. X. Xiao, X. Pan, X. H. Chen, R. Brunecky, J. J. Berry, K. Zhu, M. C. Beard, Z. V. Vardeny *et al.*, Spin-dependent charge transport through 2D chiral hybrid lead-iodide perovskites, *Sci. Adv.* **5**, 0571 (2019).
- [26] H. P. Lu, C. X. Xiao, R. Y. Song, T. Y. Li, A. E. Maughan, A. Levin, R. Brunecky, J. J. Berry, D. B. Mitzi, V. Blum *et al.*, Highly distorted chiral two-dimensional tin iodide perovskites for spin polarized charge transport, *J. Am. Chem. Soc.* **142**, 13030 (2020).
- [27] J. Gersten, K. Kaasbjerg, and A. Nitzan, Induced spin filtering in electron transmission through chiral molecular layers adsorbed on metals with strong spin-orbit coupling, *J. Chem. Phys.* **139**, 114111 (2013).
- [28] E. Medina, F. López, M. A. Ratner, and V. Mujica, Chiral molecular films as electron polarizers and polarization modulators, *Europhys. Lett.* **99**, 17006 (2012).
- [29] Y. Z. Liu, J. W. Xiao, J. Koo, and B. H. Yan, Chirality-driven topological electronic structure of DNA-like materials, *Nat. Mater.* **20**, 638 (2021).
- [30] R. Gutierrez, E. Díaz, R. Naaman, and G. Cuniberti, Spin-selective transport through helical molecular systems, *Phys. Rev. B* **85**, 081404(R) (2012).
- [31] R. Gutierrez, E. Díaz, C. Gaul, T. Brumme, F. Domínguez-Adame, and G. Cuniberti, Modeling spin transport in helical fields: Derivation of an effective low-dimensional Hamiltonian, *J. Phys. Chem. C* **117**, 22276 (2013).
- [32] A. M. Guo and Q. F. Sun, Spin-selective transport of electrons in DNA double helix, *Phys. Rev. Lett.* **108**, 218102 (2012).
- [33] A. M. Guo and Q. F. Sun, Sequence-dependent spin-selective tunneling along double-stranded DNA, *Phys. Rev. B* **86**, 115441 (2012).
- [34] A. M. Guo and Q. F. Sun, Spin-dependent electron transport in protein-like single-helical molecules, *Proc. Natl. Acad. Sci. USA* **111**, 11658 (2014).
- [35] K. Shiota, A. Inui, Y. Hosaka, R. Amano, Y. Ōnuki, M. Hedo, T. Nakama, D. Hirobe, J.-i. Ohe, J.-i. Kishine *et al.*, Chirality-induced spin polarization over macroscopic distances in chiral disilicide crystals, *Phys. Rev. Lett.* **127**, 126602 (2021).
- [36] H. Shishido, R. Sakai, Y. Hosaka, and Y. Togawa, Detection of chirality-induced spin polarization over millimeters in polycrystalline bulk samples of chiral disilicides NbSi₂ and TaSi₂, *Appl. Phys. Lett.* **119**, 182403 (2021).
- [37] A. Roy, F. T. Cerasoli, A. Jayaraj, K. Tenzin, M. B. Nardelli, and J. Sławińska, Long-range current-induced spin accumulation in chiral crystals, *npj Comput. Mater.* **8**, 243 (2022).
- [38] Y. Ōnuki, A. Nakamura, T. Uejo, A. Teruya, M. Hedo, T. Nakama, F. Honda, and H. Harima, Chiral-structure-driven split Fermi surface properties in TaSi₂, NbSi₂, and VSi₂, *J. Phys. Soc. Jpn.* **83**, 061018 (2014).
- [39] S. Kontani, T. Ito, S. Kimura, A. Nakamura, M. Hedo, T. Nakama, T. Tomi, Y. Onuki, and H. Harima, in Meeting Abstracts of the Physical Society of Japan 73.2, 1020, 2018 (unpublished).
- [40] C. A. C. Garcia, D. M. Nenko, G. Varnavides, and P. Narang, Anisotropic phonon-mediated electronic transport in chiral Weyl semimetals, *Phys. Rev. Mater.* **5**, L091202 (2021).
- [41] Y. Kousaka, T. Sayo, S. Iwasaki, R. Saki, C. Shimada, H. Shishido, and Y. Togawa, Chirality-selected crystal growth and spin polarization over centimeters of transition metal disilicide crystals, *Jpn. J. Appl. Phys.* **62**, 015506 (2023).
- [42] G. Kresse and J. Furthmüller, Efficient iterative schemes for *ab initio* total-energy calculations using a plane-wave basis set, *Phys. Rev. B* **54**, 11169 (1996).
- [43] P. E. Blöchl, Projector augmented wave method, *Phys. Rev. B* **50**, 17953 (1994).
- [44] G. Kresse and D. Joubert, From ultrasoft pseudopotentials to the projector augmented-wave method, *Phys. Rev. B* **59**, 1758 (1999).
- [45] J. P. Perdew, K. Burke, and M. Ernzerhof, Generalized gradient approximation made simple, *Phys. Rev. Lett.* **77**, 3865 (1996).
- [46] H. Sakamoto, A. Fujii, K. Tanaka, and H. Inui, Enantiomorph identification of transition-metal disilicides with the C40 structure (the space group of *P*₆₂₂ and *P*₆₄₂₂) by new convergent-beam electron diffraction method, *Acta Mater.* **53**, 41 (2005).
- [47] M. X. Chen and M. Weinert, Layer *k*-projection and unfolding electronic bands at interfaces, *Phys. Rev. B* **98**, 245421 (2018).
- [48] See Supplemental Material at <http://link.aps.org/supplemental/10.1103/PhysRevB.108.235164> for movies with additional experimental data.
- [49] H. F. Yang, K. Y. He, J. Koo, S. W. Shen, S. H. Zhang, G. Liu, Y. Z. Liu, C. Chen, A. J. Liang, K. Huang *et al.*, Visualization of chiral electronic structure and anomalous optical response in a material with chiral charge density waves, *Phys. Rev. Lett.* **129**, 156401 (2022).
- [50] S. S. Tsirkin, I. Souza, and D. Vanderbilt, Composite Weyl nodes stabilized by screw symmetry with and without time-reversal invariance, *Phys. Rev. B* **96**, 045102 (2017).